



## High-precision studies of the soft dipole mode in two-neutron halo nuclei: The ${}^6\text{He}$ case

L. V. Grigorenko <sup>1,2,3,\*</sup>, N. B. Shulgina <sup>3,4</sup> and M. V. Zhukov<sup>5</sup>

<sup>1</sup>*Flerov Laboratory of Nuclear Reactions, JINR, 141980 Dubna, Russia*

<sup>2</sup>*National Research Nuclear University “MEPhI”, 115409 Moscow, Russia*

<sup>3</sup>*National Research Centre “Kurchatov Institute”, Kurchatov sq. 1, 123182 Moscow, Russia*

<sup>4</sup>*Bogoliubov Laboratory of Theoretical Physics, JINR, 141980 Dubna, Russia*

<sup>5</sup>*Department of Physics, Chalmers University of Technology, 41296 Göteborg, Sweden*



(Received 30 March 2020; accepted 24 June 2020; published 14 July 2020)

The soft dipole  $E1$  strength function is calculated for the transition from the  ${}^6\text{He}$   $0^+$  ground state to the  $1^-$  continuum  ${}^4\text{He} + n + n$ . The calculations were performed within the hyperspherical harmonics formalism. The sensitivity of the results to the  ${}^6\text{He}$  ground-state structure and to final-state interactions, are analyzed. The large-basis calculations show the reliably converged results for soft dipole strength function and for momentum correlations of the  ${}^6\text{He} \rightarrow {}^4\text{He} + n + n$  dissociation products. Transition mechanisms are analyzed based on the momentum correlations. The comparison with experimental data is provided.

DOI: [10.1103/PhysRevC.102.014611](https://doi.org/10.1103/PhysRevC.102.014611)

### I. INTRODUCTION

The basic idea of the soft dipole mode (SDM) is quite simple. The wave function (WF) of a weakly bound state has long asymptotic tail spreading in the classically forbidden region (nucleon halo). Acting on such a WF by electromagnetic operator (with a power dependence on radius) further enhances the asymptotic region and we get a very long-range source, which populates the continuum. In this situation the transition matrix element may get noticeable low-energy enhancement even in the case of smooth (nonresonant) continuum in the final state. For one-neutron halos this scenario becomes important for binding energies smaller than 1 MeV, providing the peak in the  $E1$  strength function (SF) at decay energies smaller than 1 MeV.

We would like to begin this paper with a terminological note, which in reality is deeply connected with the essence of the discussed problem. There exists certain controversy about the idea of the SDM on which we would like to dwell a little. Sometimes this phenomenon is characterized as soft dipole resonance. Such a notion contradicts the standard vision of resonance as an entity, which is totally independent of the population mechanism. It stems, however, from vision of the SDM as a low-energy offspring of the giant dipole resonance (GDR). The GDR phenomenon is not, strictly speaking, resonance itself, but it unifies resonances of certain collective nature clustering in the certain energy range. The two-body SDM evidently does not belong to this realm being a single-particle geometric phenomenon. In contrast, the Pigmi dipole resonance (PDR) [1,2] can be seen as a true collective excitation connected with several neutrons contributing to formation of neutron skin. In any case it should be understood

that the existence of both the SDM and the PDR excitations is based on the separation of scales in the nucleon WF. These are radial scales of halo nucleons (or skin nucleons) WF and radial scale of the bulk of nucleons. The bulk of nucleons contributes to GDR formation, while the nucleons of halo (or skin) produce the sizable low-energy enhancement in the  $E1$  strength function: SDM (or PDR).

In contrast to the one-neutron halo case, the SDM in the case of three-cluster systems (two-nucleon halos) is quite complicated. (i) The SDM in the three-cluster systems can not be attributed entirely to initial state geometry as in the two-body case. The continuum dynamics in this case can not be neglected if we would like to produce a decent approximation to the real situation. (ii) The continuum dynamics in this case is an entangled mixture of resonant and nonresonant dynamics. Qualitatively, in the odd-parity continuum one of the nucleons populates a natural parity state where it has strong resonating interaction with core ( $l = 1$  for  ${}^6\text{He}$ ), while the other nucleon is in nonresonating non-natural parity state (e.g.,  $l = 0, 2$  for  ${}^6\text{He}$ ), see Fig. 1(b) for illustration. Thus the three-body SDM can be seen as a collective phenomenon with only valence nucleons involved in the collective motion. This form of continuum dynamics is especially difficult for treatment and demands high calculation accuracy.

The soft dipole excitations of  ${}^6\text{He}$  were studied theoretically by different methods [3–11]. Shortcomings of these studies will be discussed later in present paper. We obtain accurate fully converged results for  $E1$  SF and well-converged results for three-body correlations. Reliable convergence allows us to understand a lot of problematic issues of the previous studies. An important aspect of the analysis illustrated in Fig. 1(a) is the transition from three-body dynamics of SDM at low energies ( $E_T \lesssim 1$  MeV) to semisequential dynamics at high energies ( $E_T \gtrsim 2.5$  MeV); three-body energy  $E_T$  is defined relative to the three-body breakup threshold.

\*lgrigorenko@yandex.ru

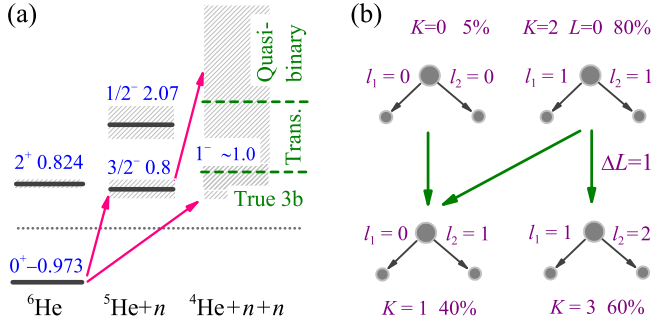


FIG. 1. (a) Energy levels of  ${}^6\text{He}$  (left),  ${}^5\text{He}$  (middle), and (right) population mechanisms for the soft dipole excitation in  ${}^6\text{He}$  at different energies. (b) Population of the major configurations of the SDM source (10) from the major configurations of the  ${}^6\text{He}$  g.s. WF (8).

The only experimental data available for the  ${}^6\text{He} \rightarrow {}^4\text{He}+n+n$  dissociation is the studies of Ref. [12]. This material was further elaborated in the review paper [13]. The three-body correlation aspect of these data was analyzed in Ref. [14]. The data are over 20 years old and quality of them is not very high. It is also important to note that a lot of experimental efforts were dedicated to the SDM in  ${}^{11}\text{Li}$ . The general experimental situation regarding the Coulomb dissociation of  ${}^{11}\text{Li}$  is quite controversial ([15] and references therein). More recent experimental results on different inelastic excitations of  ${}^{11}\text{Li}$  [16,17] support the idea of very pronounced SDM in  ${}^{11}\text{Li}$  but do not allow full quantitative description. The  ${}^6\text{He}$  nucleus could have been a reference case for SDM studies in the three-cluster systems, but very detailed and accurate experimental data are needed, which are not available so far.

The interest to studies of SDM (or/and PDR) is partly based on the common nowadays idea that the radiative capture rates for the three-body capture processes can be based on the experimentally measured Coulomb dissociation cross sections. The procedure can not be absolutely straightforward because it involves an extrapolation from intermediate energies (available experimentally) to quite low energies (contributing to the astrophysical capture rates at temperatures of astrophysical interest). The prerequisite of such an extrapolation is, of course, an accurate treatment of the  $E1$  SF. Problems of this treatment were discussed in Refs. [18,19] for the case of the  ${}^{15}\text{O}+p+p \rightarrow {}^{17}\text{Ne}+\gamma$  process. A discussion of low-energy behavior of the  $E1$  SF for the case of the  ${}^4\text{He}+n+n \rightarrow {}^6\text{He}+\gamma$  process will be given in a forthcoming paper [20].

## II. THEORETICAL MODEL

The formalism we apply here has already been used for studies of the soft dipole excitation of  ${}^{17}\text{Ne}$  in Ref. [18] and for the isovector soft dipole excitation of  ${}^6\text{Be}$  in Ref. [21]. However, it was given there briefly, so adding some more technical details is appropriate. The hyperspherical harmonics (HH) method itself has already been described in our previous works [22–24], and the details are provided here more for completeness of the description.

### A. Model for the ${}^6\text{He}$ $E1$ dissociation process

The bound  ${}^6\text{He}$  ground-state wave function is obtained in a  ${}^4\text{He}+n+n$  model by solving the homogeneous three-body Schrödinger equation (SE)

$$[\hat{H}_3 + V_3(\rho) + E_b]\Psi_{\text{gs}}^{J_i M_i} = 0,$$

$$\hat{H}_3 = \hat{T}_3 + V_{cn_1}(\mathbf{r}_{cn_1}) + V_{cn_2}(\mathbf{r}_{cn_2}) + V_{n_1 n_2}(\mathbf{r}_{n_1 n_2}), \quad (1)$$

see also Refs. [22,25,26]. The ideology of our approach is that the three-body formalism theoretically extrapolates the properties of the two-body subsystems [these are introduced via the phenomenologically defined pairwise potentials  $V_{ij}(\mathbf{r}_{ij})$ ] to the properties of the composite three-body systems. This works well for systems with developed clusterization and strongly bound clusters.  ${}^6\text{He}$  is one of the best systems appropriate for such theoretical studies. Nevertheless, this description is never perfect and for careful calculations of certain observables we need to fit the basic properties of the three-body system [binding energy for the ground state (g.s.)] to the experimental ones. For this reason phenomenological three-body potential  $V_3(\rho)$  depending on the hyperradius only is added to the Schrödinger equation.

To obtain the  $E1$  strength function we solve the following inhomogeneous SE

$$[\hat{H}_3 + \tilde{V}_3(\rho) - E_T]\Psi_{M_i m}^{JM(+)} = \mathcal{O}_{E1,m}\Psi_{\text{gs}}^{J_i M_i}. \quad (2)$$

The phenomenological three-body potential, which is appropriate for the continuum is expected to be different from that for the ground state and also somehow smaller ( $\tilde{V}_3 \lesssim V_3$ ).

Within the hyperspherical method the three-body Jacobi vectors

$$\{\mathbf{X}, \mathbf{Y}\} = \{X, \Omega_x, Y, \Omega_y\},$$

and corresponding hyperspherical variables in coordinate space

$$\{\rho, \Omega_\rho\}, \quad \Omega_\rho = \{\theta_\rho, \Omega_x, \Omega_y\},$$

are defined as

$$\mathbf{X} = \mathbf{r}_1 - \mathbf{r}_2, \quad \mathbf{Y} = \frac{A_1 \mathbf{r}_1 + A_2 \mathbf{r}_2}{A_1 + A_2} - \mathbf{r}_3, \quad (3)$$

$$\begin{aligned} \rho^2 &= \frac{A_1 A_2}{A_1 + A_2} X^2 + \frac{(A_1 + A_2) A_3}{A} Y^2 \\ &= (A_1 A_2 r_{12}^2 + A_2 A_3 r_{23}^2 + A_3 A_1 r_{31}^2) / A, \end{aligned} \quad (4)$$

$$\theta_\rho = \arctan \left[ \sqrt{\frac{A_1 A_2 A}{A_3 (A_1 + A_2)^2}} \frac{X}{Y} \right], \quad (5)$$

where  $A = A_1 + A_2 + A_3$ . The three-body Schrödinger equations for core+ $N+N$  systems are solved in the so-called T Jacobi system (core is particle number 3). Jacobi vectors and hyperangle  $\theta_\rho$  in the other Jacobi systems can be obtained by cyclic permutations of the cluster coordinates and mass numbers. The hyperradius  $\rho$  is invariant under permutations, see Eq. (4).

The  $E1$  transition operator has the following definition and relation to the dipole operator

$$\mathcal{O}_{E1,m} = e \sum_{i=1,3} Z_i r_i Y_{1m}(\hat{r}_i) = \sqrt{\frac{3}{4\pi}} D_m,$$

where  $\mathbf{D} = \sum_{i=1,3} e Z_i \mathbf{r}_i$ . Attention should be paid on a misprint in the definition of this operator in Ref. [19], which, however, did not affect the results of this paper. For two-neutron halo case of  ${}^6\text{He}$  the dipole operator acts on the core particle only

$$\begin{aligned} \mathcal{O}_{E1,m} &= e Z_3 r_3 Y_{1m}(\hat{r}_3) = Z_{\text{eff}} \rho \cos(\theta_\rho) Y_{1m}(\hat{y}), \\ Z_{\text{eff}}^2 &= \frac{e^2 Z_3^2 (A_1 + A_2)}{A_3(A_1 + A_2 + A_3)} = \frac{e^2}{3}. \end{aligned} \quad (6)$$

For two-proton case this is also true, but with effective core charge

$$Z_3 \rightarrow Z_3 - A_3,$$

because in the center-of-mass we have the relation  $A_1 \mathbf{r}_1 + A_2 \mathbf{r}_2 \equiv -A_3 \mathbf{r}_3$ .

The three-body continuum WF  $\Psi_{M,m}^{JM(+)}$  and the initial bound state WF  $\Psi_{\text{gs}}^{J_i M_i}$  are defined as

$$\Psi_{M,m}^{JM(+)} = C_{J_i M_i m}^{JM} \rho^{-5/2} \sum_{K_\gamma} \chi_{JK_\gamma}^{(+)}(\varkappa \rho) \mathcal{J}_{K_\gamma}^{JM}(\Omega_\rho), \quad (7)$$

$$\Psi_{\text{gs}}^{J_i M_i} = \rho^{-5/2} \sum_{J K_i \gamma_i} \chi_{J_i K_i \gamma_i}(\rho) \mathcal{J}_{K_i \gamma_i}^{J_i M_i}(\Omega_\rho). \quad (8)$$

The functions  $\mathcal{J}_{K_\gamma}^{JM}(\Omega_\rho)$  are hyperspherical harmonics coupled with spin functions to total spin  $J$ . Multi-index  $\gamma$  denotes the complete set of three-body quantum numbers except the principal quantum number  $K$ : for spinless core cluster  $\gamma = \{L, S, l_x, l_y\}$ .

For these WFs the Schrödinger equation (2) is reduced to a set of coupled inhomogeneous differential equations

$$\begin{aligned} \left[ \frac{d^2}{d\rho^2} - \frac{\mathcal{L}(\mathcal{L}+1)}{\rho^2} - 2M(E_T - V_{K_\gamma, K_\gamma}(\rho)) \right] \chi_{JK_\gamma}^{(+)}(\varkappa \rho) \\ = 2M \sum_{K' \gamma' \neq K_\gamma} V_{K' \gamma', K_\gamma}(\rho) \chi_{JK' \gamma'}^{(+)}(\varkappa \rho) + 2M \phi_{K_\gamma}(\rho), \end{aligned} \quad (9)$$

where  $M$  is scaling mass, taken in this work as average nucleon mass in  ${}^6\text{He}$ . The generalized angular momentum is defined by the principal hyperspherical quantum number  $K$  as

$$\mathcal{L} = K + 3/2.$$

The partial wave decomposition of the SDM source is given by

$$\begin{aligned} \phi_{K_\gamma}(\rho) &= Z_{\text{eff}} \sum_{K_i \gamma_i} \langle K_\gamma | \cos(\theta_\rho) | K_i \gamma_i \rangle \\ &\quad \times \langle J_\gamma \| Y_1(\hat{y}) \| J_i \gamma_i \rangle \rho \chi_{J_i K_i \gamma_i}(\rho). \end{aligned} \quad (10)$$

The hyperspherical and reduced angular matrix elements are

$$\begin{aligned} \langle K_\gamma | \cos(\theta) | K_i \gamma_i \rangle &= \int_0^{\pi/2} d\theta_\rho \psi_K^{l_x l_y}(\theta_\rho) \psi_{K_i}^{l_x l_y}(\theta_\rho) \sin^2(\theta_\rho) \cos^3(\theta_\rho), \\ \langle J_\gamma \| Y_1(\hat{y}) \| J_i \gamma_i \rangle &= \hat{l}_y \hat{l}_x \hat{L}^i \hat{L}^i \hat{S}^i \hat{J}^i \hat{1}^3 \delta_{S_i S} \begin{Bmatrix} l_x^i & l_y^i & L^i \\ 0 & 1 & 1 \\ l_x & l_y & L \end{Bmatrix} \begin{Bmatrix} L^i & S^i & J^i \\ 1 & 0 & 1 \\ L & S & J \end{Bmatrix} \frac{C_{l_i 0 1}^{l_i 0}}{\sqrt{4\pi}}, \end{aligned}$$

where we use the shortcut notation  $\hat{m} = \sqrt{2m+1}$ .

The asymptotic expression for the WF  $\chi_{J_f K_f \gamma_f}^{(+)}(\varkappa \rho)$  is

$$\chi_{JK_\gamma}^{(+)}(\varkappa \rho) = A_{JK_\gamma} \mathcal{H}_{\mathcal{L}}^{(+)}(\varkappa \rho).$$

Here  $\mathcal{H}_{\mathcal{L}}^{(\pm)} = \mathcal{N}_{\mathcal{L}} \pm i \mathcal{J}_{\mathcal{L}}$  are the Riccati-Bessel functions of half-integer index  $\mathcal{L}$ , with the long-range asymptotics  $\approx \exp(\pm i \varkappa \rho)$ , describing the in- and outgoing three-body spherical waves. The outgoing flux through the hypersphere of a large radius is

$$j_J = \frac{\varkappa}{M} \sum_{K_\gamma} |A_{JK_\gamma}|^2 = \sum_{K_\gamma} \sqrt{\frac{2E_T}{M}} |A_{JK_\gamma}|^2,$$

and the  $E1$  strength function is expressed via this flux as

$$\frac{dB_{E1}}{dE_T} = \frac{1}{2\pi} \sum_J \frac{2J+1}{2J_i+1} j_J. \quad (11)$$

Let us also establish a connection with more ordinary formalism expressing the  $E1$  strength function in terms of the matrix elements of the dipole operator. Within the Green's

function formalism for coupled channel differential equations the asymptotic coefficient can be expressed as

$$A_{JK_\gamma} = -\frac{2M}{\varkappa} \int d\rho \sum_{K' \gamma'} \chi_{JK_\gamma, K' \gamma'}(\varkappa \rho) \phi_{K' \gamma'}(\rho),$$

where  $\chi_{JK_\gamma, K' \gamma'}$  is the solution of the homogeneous part of Eqs. (9) diagonalizing the  $3 \rightarrow 3$  elastic scattering  $S$  matrix

$$\begin{aligned} S_{K_\gamma, K' \gamma'} &= \exp(2i\delta_{K_\gamma, K' \gamma'}), \\ \chi_{JK_\gamma, K' \gamma'}(\varkappa \rho) &= \exp(i\delta_{K_\gamma, K' \gamma'}) [\mathcal{J}_{\mathcal{L}'}(\varkappa \rho) \cos(\delta_{K_\gamma, K' \gamma'}) \\ &\quad + \mathcal{N}_{\mathcal{L}'}(\varkappa \rho) \sin(\delta_{K_\gamma, K' \gamma'})]. \end{aligned}$$

Then with definitions

$$\begin{aligned} A_{JK_\gamma} &= -\frac{2M}{\varkappa} \sqrt{\frac{\pi}{2}} M_{JK_\gamma}, \\ M_{JK_\gamma} &= \sum_{K' \gamma', K_i \gamma_i} \langle K' \gamma' | \cos(\theta) | K_i \gamma_i \rangle \langle J_\gamma' \| Y_1(\hat{y}) \| J_i \gamma_i \rangle \\ &\quad \times \int d\rho \sqrt{\frac{2}{\pi}} \chi_{JK_\gamma, K' \gamma'}(\varkappa \rho) \rho \chi_{J_i K_i \gamma_i}(\rho). \end{aligned}$$

one gets the conventional expression for the  $E1$  strength function

$$\frac{dB_{E1}}{dE_T} = \sum_J \frac{2J+1}{2J_i+1} \sum_{K\gamma} \sqrt{\frac{M}{2E_T}} |M_{JK\gamma}|^2,$$

which is equivalent to Eq. (11). However, the solution of inhomogeneous set of equations (9) is found to be technically preferable.

It is easy to find out that energy integrated value of the  $E1$  strength function is connected with the ground-state rms value of the core distance  $\langle r_3^2 \rangle$  from the center of mass of the whole three-body system.

$$\int \frac{dB_{E1}}{dE_T} dE_T = \frac{3}{4\pi} e^2 Z_3^2 \langle r_3^2 \rangle.$$

This is so-called non-energy-weighted (NEW)  $E1$  sum rule, which can be used for crosscheck of the theoretical calculations as well as for determination of the ground-state geometry from experimental data.

### B. Momentum distributions

To define momentum distributions of the three-body decay products we should introduce Jacobi vectors  $\{\mathbf{k}_x, \mathbf{k}_y\}$  in the momentum space and hyperspherical variables  $\{\mathcal{K}, \Omega_{\mathcal{K}}\}$

$$\begin{aligned} \mathbf{k}_x &= \frac{A_2}{A_1+A_2} \mathbf{k}_1 - \frac{A_1}{A_1+A_2} \mathbf{k}_2, \\ \mathbf{k}_y &= \frac{A_3}{A} (\mathbf{k}_1 + \mathbf{k}_2) - \frac{A_1+A_2}{A} \mathbf{k}_3, \\ \mathcal{K}^2 &= 2ME_T = 2M(E_x + E_y) \\ &= \frac{A_1+A_2}{A_1A_2} k_x^2 + \frac{A}{(A_1+A_2)A_3} k_y^2, \end{aligned} \quad (12)$$

$$\Omega_{\mathcal{K}} = \{\theta_{\mathcal{K}}, \Omega_{k_x}, \Omega_{k_y}\}, \quad \theta_{\mathcal{K}} = \arctan[\sqrt{E_x/E_y}]. \quad (13)$$

For the fixed decay energy, the three-body correlations are defined by five parameters of  $\Omega_{\mathcal{K}}$ . It is more practical to split the correlation space into internal correlations (relative motion of three particles) and external correlations (orientation of the three-body decay plane in the space). It is convenient to describe internal correlations with two parameters  $\{\varepsilon, \cos(\theta_k)\}$ , where  $\varepsilon$  is the energy distribution between  $X$  and  $Y$  subsystems and  $\theta_k$  is the angle between the Jacobi momenta:

$$\varepsilon = \frac{E_x}{E_T}, \quad \cos(\theta_k) = \frac{(\mathbf{k}_x, \mathbf{k}_y)}{k_x k_y}. \quad (14)$$

These parameters can be constructed in any of three Jacobi systems. The correlations constructed in different Jacobi systems are just different representations of the same physical picture. However, different aspects of the correlations may be better revealed in a particular Jacobi system. For the core+ $N$ + $N$  systems there are two nonequivalent Jacobi systems: T and Y (the correlation information for the second Y system is the same).

The external correlations are connected with spin alignment of three-body systems populated in reactions. Practical significance of such studies for the three-body systems is discussed in Refs. [27–30] and in the review [31]. No information of this kind is available for the electromagnetic dissociation

(EMD) of three-body systems and no further discussion of this topic will be provided here. However, we should emphasize that the relevant theoretical methods are already well developed and have proven to be useful in many experimental situations. So, the application of the corresponding analysis to the prospective EMD dissociation data is encouraged.

### C. Potentials

We follow potential prescription for  $A = 6$  systems, which has shown to be efficient in Refs. [22,24,25,32]. The  $NN$  potential is taken either as a simple  $s$ -wave single-Gaussian form BJ (from the book of Brown and Jackson [33])

$$V_{nn}(r) = V_0 \exp(-r^2/r_0^2), \quad (15)$$

with  $V_0 = -31$  MeV and  $r_0 = 1.8$  fm, or the realistic soft-core potential GPT (Gogny-Pires-de Tourreil [34]).

In the  $\alpha$ - $n$  channel we use an  $\ell$ -dependent potential SBB (Sack-Biedenharn-Breit [35])

$$V_{\alpha n}(r) = V_c^{(\ell)} \exp(-r^2/r_0^2) + (\mathbf{1} \cdot \mathbf{s}) V_{ls} \exp(-r^2/r_0^2), \quad (16)$$

where  $r_0 = 2.30$  fm,  $V_c^{(0)} = 50$  MeV,  $V_c^{(1)} = -47.32$  MeV,  $V_c^{(2)} = -23$  MeV, and  $V_{ls} = -11.71$  MeV.

To get the phenomenological binding-energy correction for  ${}^6\text{He}$  g.s. an additional short-range three-body potential  $V_3$  in Eq. (1) is used in the form

$$V_3(\rho) = \delta_{K\gamma, K'\gamma'} V_3^{(0)} / [1 + \exp((\rho - \rho_0)/d_3)], \quad (17)$$

where  $\rho_0 = 2.5$  fm and  $d_3 = 0.4$  fm. This short-range three-body potential (note also the small diffuseness) does not distort the interactions in the sub-barrier region, which was found to be important for consistent studies of the asymptotic WF properties, see, e.g., the discussion in Ref. [36].

We do not have clear physical motivation for introducing  $\tilde{V}_3$  in Eq. (2). However, the form this potential is taken the same as in Eq. (17) and arbitrary variation of the potential depth is used in Sec. V for studies of characteristic sensitivities of the theoretical model.

### D. ${}^6\text{He}$ ground-state wave function

Different aspect of the  ${}^6\text{He}$  g.s. WF was studied in the hyperspherical harmonics method several times [22,25]. The obtained  ${}^6\text{He}$  and  ${}^6\text{Li}$  g.s. WF were tested against various observables in several works [5,22,26,32,37,38]. They are known to provide consistent description of various long-range observables for the  ${}^6\text{He}$  and  ${}^6\text{Li}$  nuclei. The detailed account of the isobaric symmetry of  ${}^6\text{He}$  and  ${}^6\text{Be}$  g.s. can be found in Ref. [24]. For that reason we give here the most basic information about  ${}^6\text{He}$  g.s. and properties of the source function induced by the dipole operator, see Fig. 2 and Table I. In Sec. V the impact of the  ${}^6\text{He}$  g.s. WF variation on the  $E1$  SF is studied. In this section the additional information about  ${}^6\text{He}$  g.s. WF can be found, see Table II.

### E. Comment on Pauli principle treatment

The three-body description of the six-body dynamics is an approximation, used by many scientific groups all over

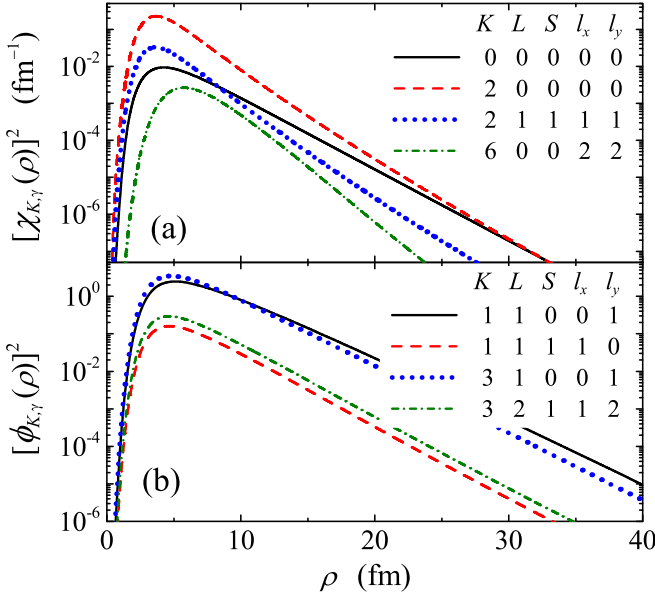


FIG. 2. Main components (squared) of the  ${}^6\text{He}$  g.s. WF (a) and the source function Eq. (10) for the  $1^-$  continuum (b).

the world for  $A = 6$  systems. In our approach Pauli principle between valence neutrons and neutrons of the  $\alpha$ -core cluster is accounted approximately. The repulsive interaction is employed in the  $s$ -wave  $\alpha$ - $n$  channel, which well reproduces the experimental  $\alpha$ - $n$  scattering phases and largely prevent valence neutrons from entering core interior. Various ways of Pauli principle treatment both approximate and exact were used in the last three decades for studies of the  $A = 6$  systems. Different approaches could be more successful for some aspects of dynamics and less to the others, but no silver bullet observable was found, which can confidently rule out some approaches.

The approximation used in this work is pragmatically justified by the mentioned above proper descriptions of various observables for  ${}^6\text{He}$  ground state. Our confidence in the three-body model applicability to  $E1$  excitation in  ${}^6\text{He}$  is strongly supported by successful studies of continuum states in  ${}^6\text{Be}$  (both resonant and nonresonant) in Refs. [21,24,30,39]. One may see in these works that even such subtle observables as very fine details of three-body correlation patterns are nicely

TABLE I. Major components of the  ${}^6\text{He}$  g.s. WF (left three columns) and major components of the source function induced by the dipole operator (right three columns). Relative probabilities  $W$  are in percent and rms hyperradii  $\langle\rho\rangle$  are in fm.

$K, L, S, l_x, l_y$	$W$	$\langle\rho\rangle$	$K, L, S, l_x, l_y$	$W$	$\langle\rho\rangle$
0 0 0 0 0	4.61	1.35	1 1 0 0 1	39.02	0.526
2 0 0 0 0	80.8	4.49	1 1 1 1 0	2.09	0.028
2 1 1 1 1	11.3	1.65	3 1 0 0 1	48.22	0.650
4 0 0 2 2	0.50	0.38	3 1 1 1 2	1.26	0.017
6 0 0 2 2	1.17	0.75	3 2 1 1 2	3.78	0.051
6 1 1 3 3	0.53	0.51	5 1 0 2 1	0.77	0.011

reproduced in the three-body model in spite of some deficiency in the Pauli principle treatment. It should be also noted that  $E1$  excitation is a very peripheral process, becoming even more peripheral in the low-energy limit. We find in this work that the major computational problems take place exactly in this energy range. This makes the antisymmetrization issue presumably not of a prime importance for the problem we study.

### III. CONVERGENCE OF SDM STRENGTH FUNCTION

The value  $K_{\text{max}}$  truncates the hyperspherical expansion in the system Eq. (9). For each  $K$  value all the possible basis states, namely all the possible combinations of  $l_x + l_y \leq K$ , are included in the HH expansion.

The SE are solved up to  $\rho_{\text{max}} = 400$  fm. The matching of the momentum distribution is performed at  $\rho_{\text{max}} = 70-90$  fm. At larger distances the artifacts of the boundary conditions begin to arise. At  $K_{\text{max}} = 25$  the number of channels reaches 260, making further direct basis increase problematic. The basis size can be effectively increased using the adiabatic procedure based on the so-called Feshbach reduction (FR) [24,36]. Feshbach reduction eliminates from the total WF  $\Psi = \Psi_p + \Psi_q$ , an arbitrary subspace  $q$  using the Green's function of this subspace:

$$H_p = T_p + V_p - V_{pq}G_qV_{pq}. \quad (18)$$

In an adiabatic approximation, we can assume that the kinetic energy term is small compared to the centrifugal barrier in the channels where this barrier is large (these are evidently the channels with large  $K$  values) and can be approximated by a constant (Feshbach energy  $E_f$ ). In this approximation the Green's function for the  $q$  subspace can be defined by matrix inversion from

$$(H - E_T)_{K\gamma, K'\gamma'} = \left[ E_f - E_T + \frac{\mathcal{L}(\mathcal{L} + 1)}{2M\rho^2} \right] \delta_{K\gamma, K'\gamma'} + V_{K\gamma, K'\gamma'} \\ = G_{K\gamma, K'\gamma'}^{-1}. \quad (19)$$

In this way the FR procedure is reduced to the construction of effective three-body interactions

$$V_{K\gamma, K'\gamma'}^{\text{eff}} = V_{K\gamma, K'\gamma'} - \sum_{\bar{K}\bar{\gamma}, \bar{K}'\bar{\gamma}'} V_{K\gamma, \bar{K}\bar{\gamma}} G_{\bar{K}\bar{\gamma}, \bar{K}'\bar{\gamma}'} V_{\bar{K}'\bar{\gamma}', K'\gamma'}. \quad (20)$$

Summations over indexes with the bar are carried out for the eliminated channels (the  $q$  subspace). Technically, we eliminate all the channels with  $K > K_{FR}$ , and the  $K_{FR}$  value defines the sector of the HH basis where the calculations remains fully dynamical. We take  $E_f \equiv E_T$  in our calculations as no significant sensitivity to this parameter in a broad variation range was found.

There are two forms of convergence to be studied to control the reliability of the FR procedure. (i) One can gradually reduce  $K_{\text{max}}$  value for the fixed  $K_{FR}$  value taken as maximum attainable in the dynamic calculations. (ii) For the maximum achieved  $K_{\text{max}}$  value one can gradually reduce  $K_{FR}$  value (using smaller and smaller dynamic basis size). The calculations of the strength function for wide  $E_T$  energy range is defined entirely by the  $K_{\text{max}}$  value. The basis size for the dynamical calculations can be taken as very modest

TABLE II. Properties of different versions of the  ${}^6\text{He}$  g.s. WFs. Energies are in MeV. The radial characteristics show root mean square values;  $\langle r_\alpha \rangle \equiv \langle r_3 \rangle$  is the rms distance from  $\alpha$  cluster to  ${}^6\text{He}$  c.m. The last two columns show the  $E1$  NEW sum rule value for  $E_T < 3$  MeV and the total value in  $\text{e}^2\text{fm}^2$  units.

Calculation	$E_b$	$\langle \rho \rangle$	$\langle r_\alpha \rangle$	$\langle r_{m1} \rangle$	$\Delta E_{\text{Coul}}$	$r_{\text{mat}}$	$r_{\text{ch}}$	$S_{\text{NEW}}^{(3)}$	$S_{\text{NEW}}^{(\infty)}$
GPT $n$ - $n$	0.973	5.16	1.17	4.50	2.302	2.43	2.019	0.568	1.307
GPT $n$ - $n$ , strong $V_3$	1.1	5.02	1.14	4.41	2.400	2.39	2.002	0.514	1.241
GPT $n$ - $n$ , weak $V_3$	0.85	5.24	1.19	4.57	2.251	2.46	2.031	0.630	1.352
BJ $n$ - $n$	0.973	5.10	1.15	4.48	2.345	2.41	2.008	0.562	1.262
Mod. strong BJ $n$ - $n$	0.973	5.53	1.31	4.52	2.095	2.57	2.103	0.854	1.639
Mod. weak BJ $n$ - $n$	0.973	4.66	0.99	4.44	2.680	2.26	1.922	0.317	0.936
As in Ref. [22]	0.973	5.49	1.23	4.88	2.111	2.54	2.048	0.672	1.445
Experiment	0.973				2.344	2.30(7) [43] 2.48(3) [45]	2.068(11) [44]	0.45(12) [12]	

$K_{FR} = 13$ – $15$  without deterioration of the SF quality. However, the majority of the presented calculations were performed with  $K_{FR} = 25$ , which is a very reliable value. The largest basis size is really needed (for  $E_T > 0.4$  MeV) for calculations of the correlation patterns in the  $\alpha + n + n$  continuum since the convergence for the correlations appears to be essentially slower than for the strength function. These aspects of the convergence is discussed in Sec. IV B 2.

The convergence trends for small and large basis sizes are illustrated in Figs. 3 and 4. We may see the following important trends in the convergence patterns.

(i) The easiest way to get converged calculations is to remove FSI. The convergence here is defined by convergence of the source function expansion, which is practically achieved at  $K_{\text{max}} = 5$ – $7$ , see Table I.

(ii) The convergence of test calculations with  $n$ - $n$  FSI switched off is achieved at  $K_{\text{max}} = 30$ – $40$ . The conditions for calculations with full three-body FSI is much worse, and complete convergence is achieved at  $K_{\text{max}} = 60$ – $70$ . The maximum basis size used in the calculations  $K_{\text{max}} = 101$ , which is very safe value for the SF calculations at  $E_T > 0.4$  MeV.

(iii) There is some form of systematic wavy behavior of the strength function in the process of convergence. It seems that for small basis sizes the SF oscillates around the final converged value. When the basis is increased, these oscillations

are shifted toward smaller energies and the magnitude of the oscillations decreases. This form of the wavy behavior can be connected with some kind of internal reflections in the system of three particles, which arise as an artifact of boundary conditions treatment in the situation of the basis truncation.

(iv) Analogous picture of convergence spoiling the low-energy part of the  $E1$  SF was observed in the three-body calculations of SDM in  ${}^{17}\text{Ne}$  [18]. The cure for this problem was found in use of a model with simplified Hamiltonian (without  $p$ - $p$  FSI), which allowed us to use the exact three-body Green's function providing precise SF treatment [18,19]. Application of such a model is based on the fact that  $p$ - $p$  FSI was found to be not important for the low-energy  $E1$  SF calculations. In  ${}^6\text{He}$  this option is evidently not available, since there is very large difference between calculations with and without  $n$ - $n$  FSI.

(v) Although the wavy behavior can be seen in Fig. 3 the position of peak in SF and the behavior of the SF low-energy slope visually stabilize at  $K_{\text{max}} \approx 30$ . For the basis sizes achieved, these artificial waves are shifted to  $E_T < 0.4$  MeV. The aspect of the low-energy SF convergence is quite intriguing and it is discussed separately in Ref. [20].

Comparison of calculations performed with quasirealistic GPT  $n$ - $n$  potential and with simple central BJ  $n$ - $n$  potential

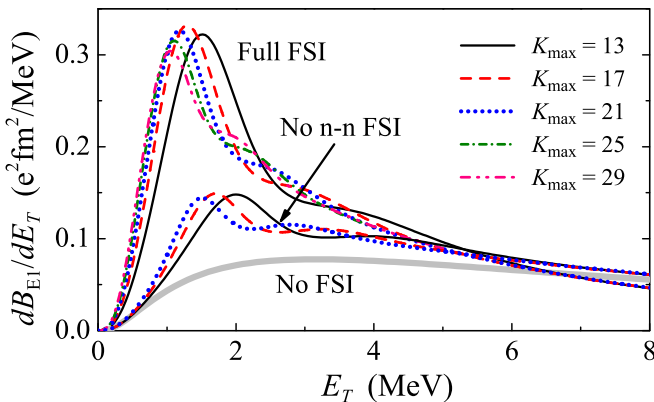


FIG. 3. Convergence of the  $E1$  strength function calculations with and without  $n$ - $n$  FSI for  $K_{\text{max}} < 30$ .

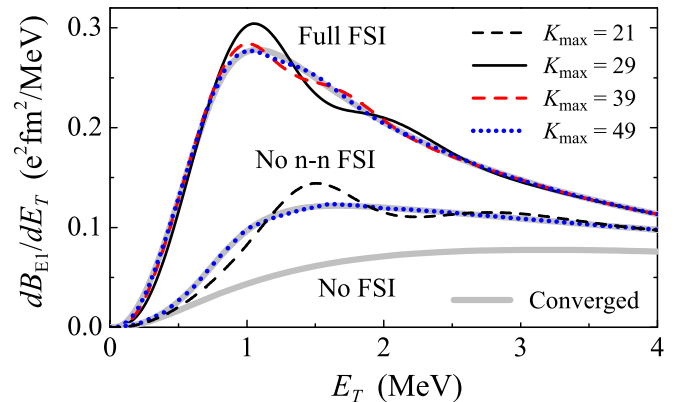


FIG. 4. Convergence of the  $E1$  strength function calculations with and without  $n$ - $n$  FSI for  $K_{\text{max}} > 30$ .

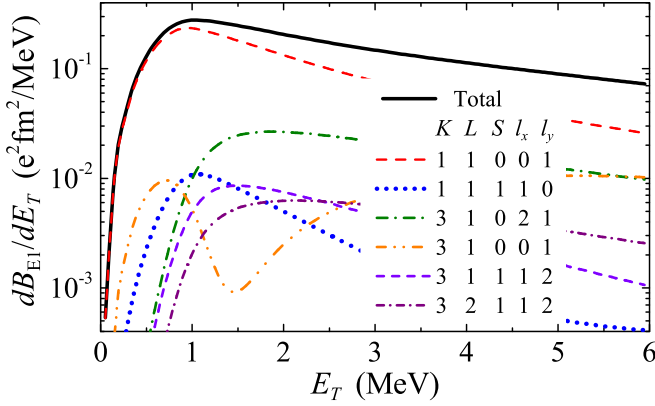


FIG. 5. The dominating contributions to the  $E1$  strength function.

provides very close results. This is a clear consequence of an extreme peripheral character of the SDM dynamics. However, the convergence of calculations with GPT potential is much slower. For that reason the largest-basis calculations were performed with the central  $n$ - $n$  potential only.

#### IV. SDM DECAY DYNAMICS

The partial wave decomposition of the  ${}^6\text{He}$  SDM SF is shown in Fig. 5. The low-energy part of the SF below  $E_T = 1$  MeV is strongly dominated by the lowest hyperspherical component  $\{K, \gamma\} = \{1, 1, 0, 0, 1\}$ . Sometimes this fact is interpreted as an opportunity to use only one channel (lowest possible channel with  $K = 1$ ) in calculations of SDM. However, this is not the case: although the relative weights of higher- $K$  channels are small, their cumulative effects to a large extent determine the magnitude of the  $K = 1$  component in the low-energy domain.

The decay dynamics of the soft dipole mode can be clarified by momentum distribution analysis of the decay products. The energy evolution of the complete (energy-angular) three-body correlation patterns for  ${}^6\text{He}$  SDM is illustrated in Fig. 6 for different decay energies. The inclusive energy distributions are shown in Figs. 7, 8, 9, and 12. It can be found that correlation patterns are qualitatively different in three regions: (i)  $E_T \lesssim 1$  MeV, (ii)  $1 \lesssim E_T \lesssim 2.5$  MeV, (iii)  $2.5 \lesssim E_T$  MeV.

##### A. True three-body decay dynamics

The region (i) with  $E_T \lesssim 1$  MeV corresponds to so-called true three-body emission. This is a situation of essentially collective three-body motion. Technically, it is expected that such a motion is well described by a small number of HH terms. In the low-energy limit it should be just one term with  $K = K_{\min} = l_x(\min) + l_y(\min)$ , most likely, the lowest hyperspherical term (or, possibly, terms for  $K_{\min} > 0$ ). The corresponding correlation pattern is called three-body phase volume and it has meaning of phase volume corrected for angular momenta. For single HH with definite  $l_x$  and  $l_y$  values the three-body phase space is

$$dW/d\varepsilon \approx \sqrt{\varepsilon^{1+2l_x}(1-\varepsilon)^{1+2l_y}}. \quad (21)$$

It can be seen in Fig. 7 that in the low-energy limit the energy distribution in the Jacobi T system tends to phase volume for  $[sp]$  configuration with  $l_x = 0$  and  $l_y = 1$

$$dW/d\varepsilon \approx \sqrt{\varepsilon(1-\varepsilon)^3}. \quad (22)$$

For the “no  $n$ - $n$  FSI” calculations this is exactly true for  $E_T \lesssim 0.3$  MeV. In full three-body case there is a strong enhancement of the low-energy part of the distribution due to the dineutron FSI. This effect is important even at energy as low as  $E_T \approx$

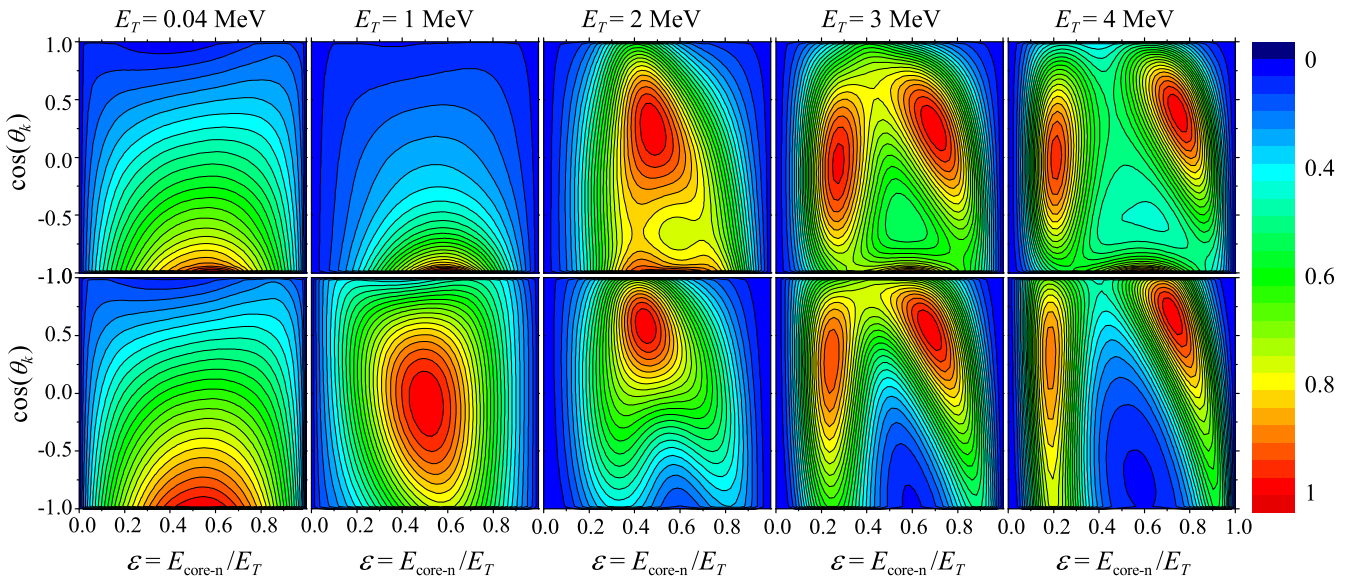


FIG. 6. Complete energy-angular three-body correlations for  ${}^6\text{He}$  SDM transitions in the Y Jacobi systems. Top row corresponds to the full three-body calculation; bottom row corresponds to calculation without  $n$ - $n$  FSI. The columns correspond to decay energies  $E_T$  equal to 0.04, 1, 2, 3, and 4 MeV.

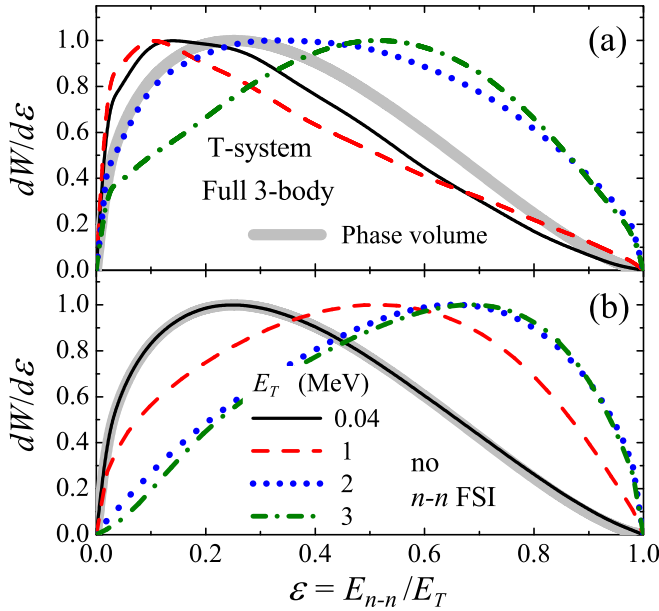


FIG. 7. Evolution of energy correlations over  $E_T$  for  ${}^6\text{He}$  SDM transitions in the T Jacobi system. (a) and (b) correspond to full three-body calculation and “no  $n$ - $n$  FSI” case, respectively. The thick gray curves show the phase volume Eq. (22).

0.04 MeV and only for  $E_T \lesssim 5$  keV the three-body phase volume behavior is retained.

In a Y Jacobi system the corresponding three-body phase volume behavior is defined by symmetry property of identical valence nucleons, which leads to  $[sp] + [ps]$  configuration mixing with almost equal weights

$$dW/d\varepsilon \approx \sqrt{\varepsilon^3(1-\varepsilon)} + \sqrt{\varepsilon(1-\varepsilon)^3} = \sqrt{\varepsilon(1-\varepsilon)}. \quad (23)$$

This expression is equivalent to the most trivial three-body  $s$ -wave phase volume ( $l_x = 0$  and  $l_y = 0$  case). It can be found in Fig. 8 that this simplistic expectation is well justified for  $E_T \lesssim 0.3$  MeV. For energies  $E_T \lesssim 1$  MeV and above the energy distribution in the Y Jacobi system tends to relatively symmetric profiles with maximum at  $\varepsilon \approx 0.5$ , which are typical for democratic decays of light  $2p$  emitters [39,40].

## B. Sequential decay dynamics

In the region (iii) with  $2.5 \lesssim E_T$  MeV the decay regime is sequential: the emission of nucleons proceed via population of the intermediate  $p_{3/2}$  resonance in the  ${}^5\text{He}$ . This can be well seen in Fig. 9 as the two-hump structure of distributions for  $E_T \gtrsim 2.5$  MeV. The sequential decay peak drifts to lower  $\varepsilon$  with  $E_T$  increase. However, it can be found from distributions of Fig. 9 that the peak with lower  $\varepsilon$  value always takes place at the same energy  $E_r = 0.84$ – $0.86$  MeV. Where this energy  $E_r$  is coming from?

### 1. Sequential peak energy

The information on the  ${}^5\text{He}$   $p_{3/2}$  resonance, governing the properties of the sequential decay, is given in Fig. 10(a). The standard description of the resonance is represented by the elastic phase shift and the corresponding elastic cross

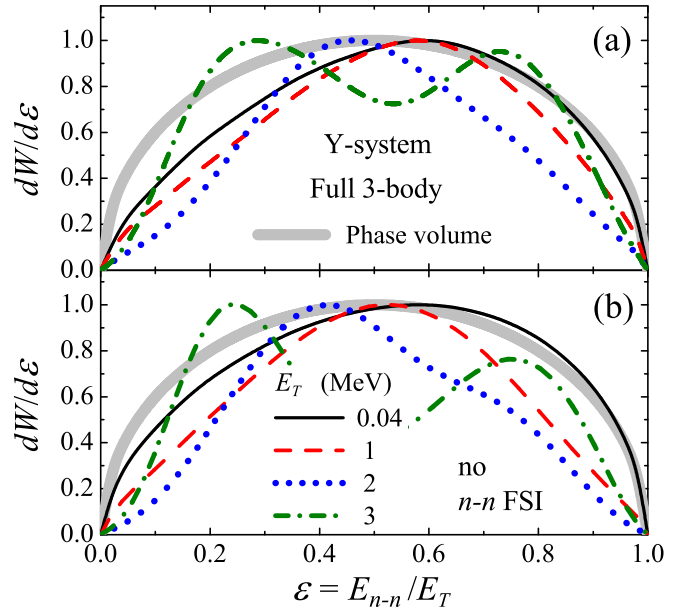


FIG. 8. Evolution of energy correlations over  $E_T$  for  ${}^6\text{He}$  SDM transitions in the Y Jacobi system. (a) and (b) correspond to full three-body calculation and “no  $n$ - $n$  FSI” case, respectively. The thick gray curves show the phase volume Eq. (23).

section. The elastic cross section for the potential used in our calculations has the peak value at  $E_r = 0.95$  MeV. However, this resonance is quite broad and we may question another continuum responses. Figure 10(b) shows also the internal

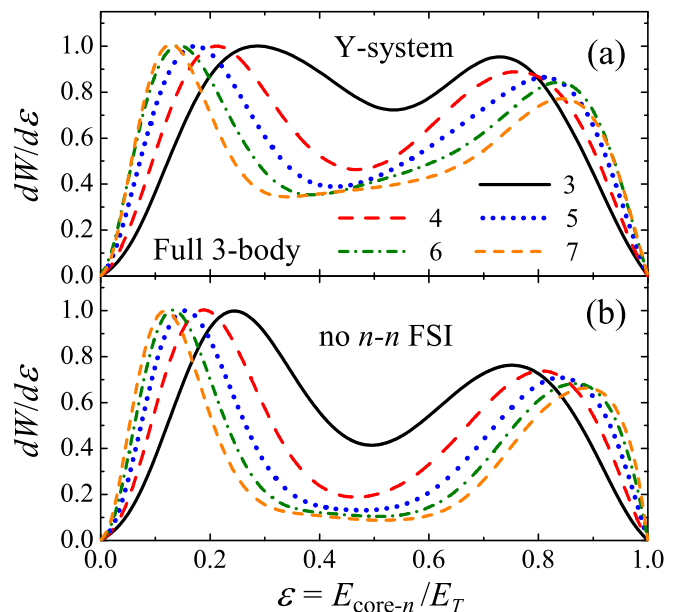


FIG. 9. Evolution of energy correlations for  ${}^6\text{He}$  SDM transitions in the Y Jacobi system for  $E_T = \{3, 4, 5, 6, 7\}$  MeV. (a) and (b) correspond to full three-body calculation and “no  $n$ - $n$  FSI” case, respectively. All the left peaks in (a) have exactly the same absolute energy  $\varepsilon E_T = 0.87$  MeV, which agrees very well with Fig. 10(b).



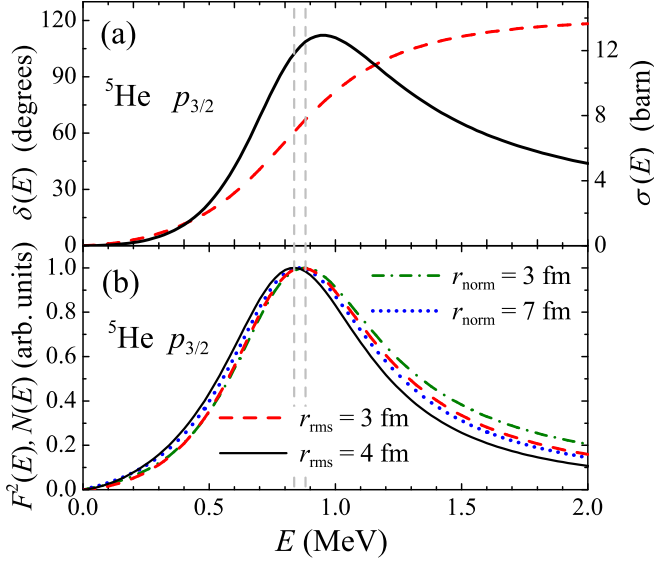


FIG. 10. Characteristics of the  ${}^5\text{He}$   $p_{3/2}$  resonance. (a) shows the phase shift and elastic cross section. (b) shows internal normalization Eq. (24) with different  $r_{\text{norm}}$  and continuum form factors Eq. (25) with different rms radii  $r_{\text{rms}}$ . Vertical dashed lines visualize positions of the highest-energy (0.83 MeV) and lowest energy (0.87 MeV) peaks in (b).

normalization

$$N_i(E) = \int_0^{r_{\text{norm}}} dr |f_i(kr)|^2, \quad (24)$$

where  $r_{\text{norm}}$  is the size of the normalization region, and continuum form factor

$$F_i(E) = \int_0^\infty dr f_i(kr)\phi(r). \quad (25)$$

Function  $f_i(kr)$  is two-body scattering WF normalized as  $\sin(kr + l\pi/2 + \delta_l)$  and the source WF  $\phi(r)$  taken in a simple analytical form (so-called Hulthen ansatz)

$$\phi(r) = \sqrt{\frac{2(r_{01} + r_{02})}{(r_{01} - r_{02})^2}} (\exp[-r/r_{01}] - \exp[-r/r_{02}]). \quad (26)$$

Here we use  $r_{01} = 0.5$  fm and vary  $r_{02}$  to get different rms radii for  $\phi(r)$ . It can be seen in Fig. 10(b) that the energies of the peak both for internal normalization and for form factors are considerably different from the peak energy of elastic cross section. The  ${}^5\text{He}$  peak energy  $E_r = 0.84\text{--}0.87$  MeV inferred from Fig. 10(b) is very stable: it has a small variation when changing the parameters in a broad range of reasonable values. This range exactly corresponds to the stable peak energies observed for different  $E_T$  in Fig. 9.

## 2. Convergence of momentum distributions

Basing on our results that we have obtained from the studies of two-nucleon emission and two-proton radioactivity we can conclude that for the energies of the resonant states the convergence is fastest, for width of this states it is slower, and for momentum correlations the convergence is the slowest [36].

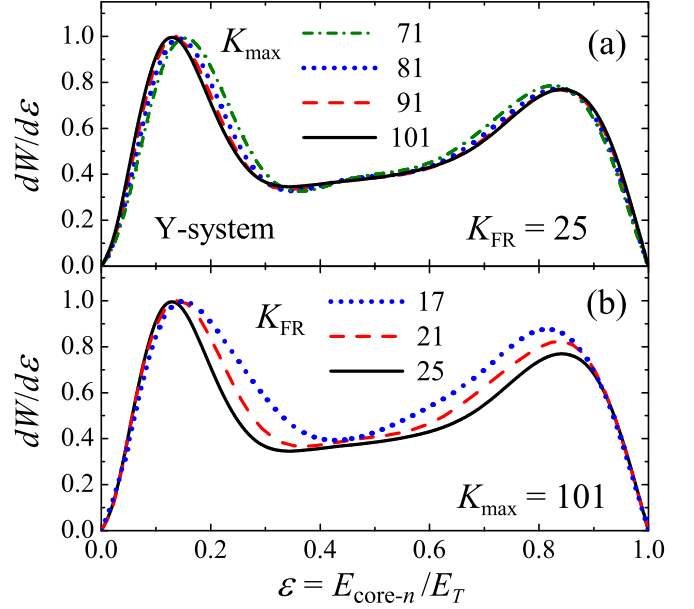


FIG. 11. Convergence of the energy distributions in the Y-coordinate system for  $E_T = 7$  MeV. (a)  $K_{\text{max}}$  convergence for fixed  $K_{\text{FR}} = 25$ . (b)  $K_{\text{FR}}$  convergence for fixed  $K_{\text{max}} = 101$ .

We can find in Figs. 3 and 4 that the convergence of strength function is very good for  $K_{\text{max}} > 50$  in a broad energy domain. If we look at the high-energy part of SF with  $E_T > 5$  MeV, the result is well converged already at very small basis sizes  $K_{\text{max}} \approx 13\text{--}15$ . In contrast, the convergence of the momentum distributions for the high-energy part of the  $E1$  strength function is found to be most challenging issue: here we need to describe the long-range formation of the peaks in the distribution for sequential decay mode via the  $p_{3/2}$  resonant g.s. of  ${}^5\text{He}$ . Extremely large basis sizes are required for that. It can be seen in Fig. 11 that the convergence is reasonably good, but not quite achieved yet. This figure illustrates  $E_T = 7$  MeV case; for  $E_T = 3\text{--}5$  MeV the convergence is much better and it is perfect for the lower energies.

## 3. Antidineutron correlation

The energy correlations in the Jacobi T system at energies  $E_T \gtrsim 2.5$  MeV are shown in Fig. 12. We can see that in contrast to the dineutron peak in the energy distribution at low  $E_T$ , a peculiar repulsive anticorrelation takes place here between neutrons. In the calculations without  $n$ - $n$  FSI there is strong suppression of probability for  $\varepsilon \lesssim 0.2$ . In full three-body calculation the  $n$ - $n$  FSI try to compensate this effective repulsion somehow. The energy distribution even has a sharp increase at  $\varepsilon \rightarrow 0$ . However, the intensity of the  $n$ - $n$  FSI is not sufficient to overcome the overall repulsive trend: the probability for  $\varepsilon \lesssim 0.2\text{--}0.3$  is still seriously suppressed.

## C. Transitional decay dynamics

In the region (ii) with  $1 \lesssim E_T \lesssim 2.5$  MeV the transition from true three-body to sequential emission dynamics is taking place. Estimates show that from the penetrability point

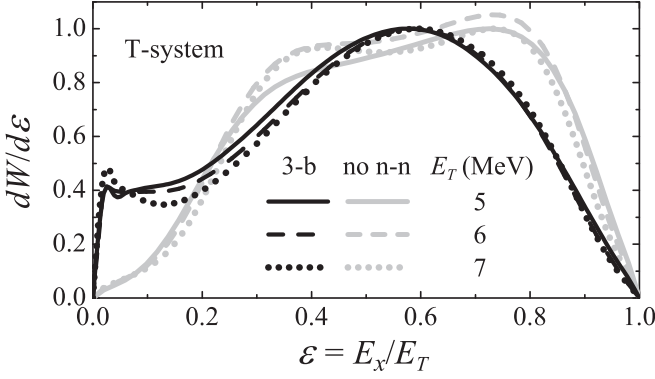


FIG. 12. Evolution of energy correlations for  ${}^6\text{He}$  SDM transitions in the T Jacobi system for  $E_T = \{5, 6, 7\}$  MeV for the full three-body calculation (black curves) and “no  $n$ - $n$  FSI” case (gray curves).

of view the turnover to sequential emission regime (via the  $p_{3/2}$  resonance in the  ${}^5\text{He}$ ) should take place at  $E_T \gtrsim 1.2$ – $1.5$  MeV. However, at energies  $E_T \approx 1.8$  MeV, the energies of the first and the second emitted neutrons with respect to the  $\alpha$  core are nearly equal, and, thus, both these nucleons can well populate the  ${}^5\text{He}$   $p_{3/2}$  resonance via its broad wings. For that reason the sequential decay can not be formed up to  $E_T \approx 2.5$  MeV and the emission has complex three-body character. The major trends of transitional dynamics were discussed in Ref. [40]. The forms of transition we face here look analogous to transitional dynamics observed in the light  $2p$  emitters, such as  ${}^6\text{Be}$  [39] and  ${}^{16}\text{Ne}$  [41,42] (so-called democratic decay).

The transition from the three-body to sequential regime is characterized by a rapid qualitative change of the correlation patterns, see Fig. 6. This is well illustrated by energy distribution changes in Figs. 7 and 8. Two most important effects are taking place in the transitional energy range.

(i) The dineutron correlation between emitted neutrons (enhancement at low  $\varepsilon$  values) typical for the low-energy  $E_T$  range is dissolved, and replaced with antidineutron correlation (depression at low  $\varepsilon$  values), as discussed above in Sec. IV B 3.

(ii) The sequential decay patterns for population of the intermediate  $p_{3/2}$  resonance in  ${}^5\text{He}$  are formed: we start from distribution with one peak at  $\varepsilon \approx 0.5$  and end with sequential two-peak correlation pattern.

## V. WHAT CAN WE CHANGE?

Before we discuss the previous theoretical results, we ask ourselves a natural question: how stable are our predictions for  $E1$  SF. To understand it we investigated (i) the impact of the  ${}^6\text{He}$  g.s. WF variation and (ii) the impact of the three-body potential  $\tilde{V}_3$  variation, see Eq. (2). The variations are not necessarily realistic: our aim is to find out which variations of the  $E1$  SF in  ${}^6\text{He}$  are, in principle, attainable.

The basic information about different versions of the  ${}^6\text{He}$  g.s. WFs is provided in the Table II. The matter radius

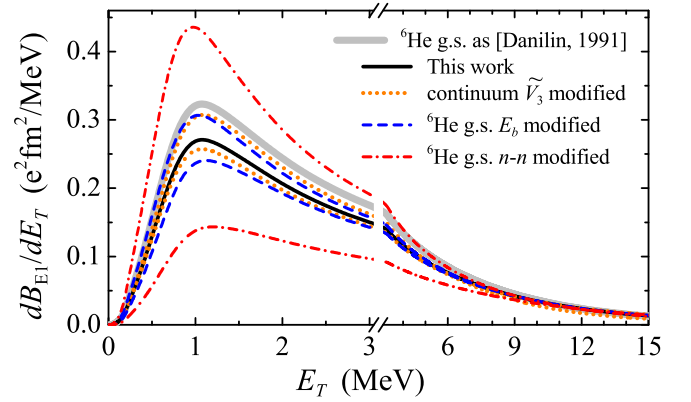


FIG. 13. What we can change by varying different aspects of the calculation.

of  ${}^6\text{He}$  is obtained as

$$6r_{\text{mat}}^2({}^6\text{He}) = \langle \rho \rangle^2 + 4r_{\text{mat}}^2({}^4\text{He}).$$

The predicted matter radius of  ${}^6\text{He}$  lies somewhere in between two values extracted from experiment, which disagree with each other and, moreover, are quite old. The most restrictive observables are the Coulomb displacement energy in  $A = 6$  isobar and the charge radius. The  $\Delta E_{\text{Coul}}$  value is reproduced nicely by our main calculation. The charge radius of  ${}^6\text{He}$ , which in the cluster model is given by

$$r_{\text{ch}}^2({}^6\text{He}) = r_{\text{ch}}^2({}^4\text{He}) + \langle r_\alpha \rangle^2 + r_{\text{ch}}^2(n),$$

is a bit underestimated. However, we can not improve agreement for this characteristic without coming to contradiction. If we somehow expand the system to get correct charge radius, the agreement for  $\Delta E_{\text{Coul}}$  will be get worse. It should be also understood that calculation of this value in the cluster model depends on a number of parameters, and not all of them are confidently defined. We use the following ingredients:  $r_{\text{ch}}(p) = 0.84$  fm,  $r_{\text{ch}}({}^4\text{He}) = 1.681$  fm,  $r_{\text{ch}}^2(n) = -0.1161$  fm, also leading to the rms matter radius of the core cluster  $r_{\text{mat}}({}^4\text{He}) = 1.495$  fm.

The  $E1$  SFs corresponding to different calculation options are collected in Fig. 13.

(i) The old  ${}^6\text{He}$  g.s. WF from Ref. [22] produces the thick gray curve in Fig. 13.

(ii) A strong variation of the  $\tilde{V}_3$  potential was performed, see Eq. (2). The orange dotted curves correspond to  $V_3^{(0)} = 32$  MeV (bottom) and  $V_3^{(0)} = -32$  MeV (top). The scale of this variation is unrealistically large. For example, for the  ${}^6\text{He}$  g.s. calculations the parameter  $V_3^{(0)} = -13.5$  MeV is used to adjust the binding energy to have exactly experimental value. We think that such variations of  $\tilde{V}_3$  is much larger than any reasonable value: the many-body effects beyond the three-cluster approximation are expected to be smaller in  $1^-$  continuum, compared to  $0^+$  g.s.

(iii) The binding energy  $E_b$  of  ${}^6\text{He}$  was varied by changing  $V_3$  potential, see Eq. (1). The blue dashed curves correspond to  $E_b = 1.1$  MeV (bottom) and  $E_b = 0.85$  MeV (top).

(iv) The geometry of the  ${}^6\text{He}$  g.s. WF has been modified using stronger and weaker  $V_m$  potentials. Red dash-dotted

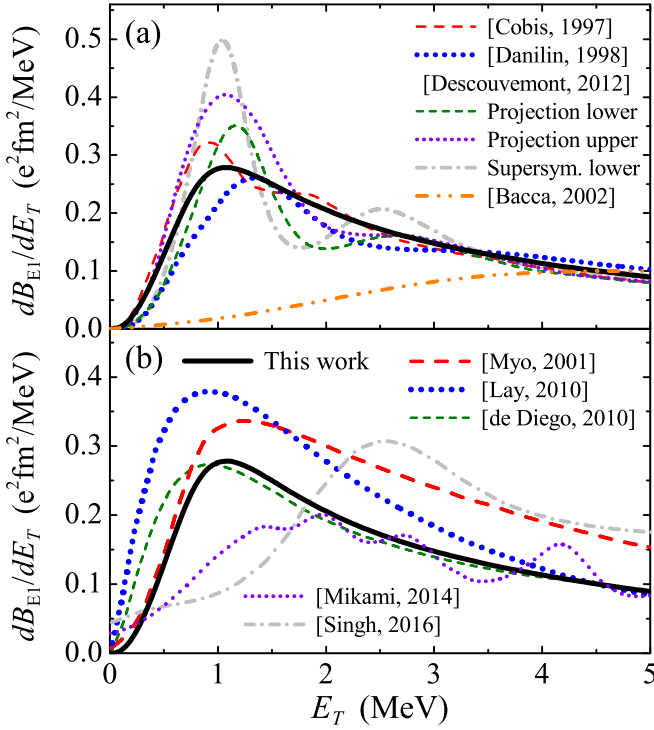


FIG. 14. Comparison of the results for the  $^6\text{He}$  E1 SF obtained in present work with the previous calculations. (a) shows the results of HH and HH-based methods [4,5,9,46]. (b) shows the results of methods based on continuum discretization [6–8,11,47].

curves show the results with  $^6\text{He}$  WF obtained with BJ potential [see Eq. (15)] with  $V_0 = -21$  MeV (bottom) and  $V_0 = -36$  MeV (top), instead of the standard value  $V_0 = -31$  MeV. The average angle between neutrons (as seen from the  $\alpha$  core) can be calculated as  $60^\circ$ ,  $66^\circ$ , and  $74^\circ$  for strong, normal, and weak  $n$ - $n$  potentials.

It can be understood from Fig. 13 and Table II that the result for E1 SF is quite stable. For variations (i)–(iii) of parameters far beyond realistic we get a modest change in the SF, which is mainly just scaling within  $\pm(10\text{--}15)\%$ . To change the theoretical prediction considerably [case (iv)], we need to change basic geometry of the  $^6\text{He}$  g.s. WF. This can hardly be compatible with our common understanding of structure, reactions, and observables for  $A = 6$  isobar.

## VI. DISCUSSION OF PREVIOUS THEORETICAL RESULTS

Comparison of the results for the  $^6\text{He}$  E1 SF obtained in this work with the previous calculations is given in Fig. 14. Calculations [5] were performed by members of our collaboration in a very similar formalism, but with numerical limitations natural to a situation twenty years ago. The wavy profile of the SF is analogous to the results obtained in the present work with limited basis  $K_{\text{max}} = 21$ , see Fig. 3. The strength function does not match exactly ours, obtained within the same limitations, because the Pauli principle treatment in the core- $n$  channel is different in Ref. [5] (so-called Pauli projection method). Also the  $^6\text{He}$  g.s. WF used in Ref. [5] is somewhat different from ours.

The calculations of Refs. [4] show the same wavy behavior, which, as we demonstrate in this work, is a symptom of insufficient convergence. The computational methods of Ref. [4] and of present work are different, but both rely on hyperspherical expansion of WF. Therefore, we may still expect some analogy in convergence trends. The behavior of the strength function in Refs. [4] on the left slope of the peak ( $E_T \approx 0.2\text{--}0.8$  MeV) is very close to the behavior of our strength function. Basing on our experience, we do not expect that this aspect of the SF [4] changes noticeably in the case of the complete convergence.

The HH calculations of Ref. [9] again show the wavy behavior discussed above. Several calculations were presented in this work, divided in two groups by treatment of the Pauli principle in the  $\alpha$ -core channel: (i) Pauli projection and (ii) supersymmetric transformation techniques. We have selected the upper and lower results from group (i) and the lower from group (ii); the other results from this group look a bit unrealistic.

It can be seen in Fig. 14(a) that all the presented results from Ref. [9] (actually all the results of HH-based methods) are a kind of oscillating around the mean value represented by our fully converged calculations. On the other hand, it should be noted that all these methods give qualitatively very similar SFs in the low-energy range, conforming the expected

$$\frac{dB_{E1}}{dE_T} \approx E_T^3, \quad (27)$$

behavior of the E1 SF for  $^6\text{He}$ . Having this correct low-energy asymptotics is the natural feature of the HH method.

The results of Ref. [46] were obtained in the HH-based method as well. However, this is six-body approach treating photodissociation in the special framework (Lorentz integral transformation). The three-body cluster  $\alpha + n + n$  threshold is not explicitly present in this approach (only the six-body threshold) and the low-energy behavior in this channel can be provided only by the basis convergence. However, the maximum basis size achieved in this work is only  $K_{\text{max}} = 11$ , which is far not sufficient even in the three-body case, which is technically much easier. As a result the effective strength function (recalculated very approximately from the cross section given in Ref. [46]) does not demonstrate soft dipole low-energy enhancement, which takes place in some form in all other approaches.

The theoretical methods collected in Fig. 14(b) are based on different forms of the continuum discretization. The calculations of Ref. [11] (this is essentially three-body model) give a peak in the E1 SF at about 2.5 MeV, which is too different from the mainstream value of 1.0–1.1 MeV.

The six-body variational method calculations of Ref. [47] effectively takes into account different possible kinds of clusterization beside  $\alpha + n + n$ . This method provides low-energy concentration of the E1 strength at about 2 MeV, which is higher than mainstream 1.0–1.1 MeV value but can be seen as a nice result considering complexity of the approach. The low-energy spectrum below 3 MeV is based on six to eight discrete states and thus its specific profile is strongly sensitive to the smoothing procedure.

The strength function obtained in Ref. [6] has a peak at higher energy ( $E_T = 1.25$  MeV) than in present work and in the papers Ref. [4,7] ( $E_T \approx 0.9$ – $1.1$  MeV). This could be a result of incomplete accounting of the  $n$ - $n$  FSI. The peak energy in Ref. [6] is close to 1.4 MeV (value obtained in calculations without  $n$ - $n$  FSI, see Fig. 14(b)). Another worrying issue is the high-energy behavior of the SF obtained in the work [6]. The SF is shown up to 6 MeV only, but if we smoothly extrapolate it to higher energies, we can infer that the  $E1$  NEW sum rule value for this SF is around  $1.8$   $e^2\text{fm}^2$ . This value corresponds to  $r_\alpha = 1.37$  fm rms distance of  $\alpha$  cluster from the center of mass in the  ${}^6\text{He}$  g.s. This is considerably larger than  $r_\alpha = 1.17$  fm for  ${}^6\text{He}$  WF used in the present work (similar radial properties of  ${}^6\text{He}$  WF were used also in the calculations [4,7]). The rms matter radius of the  ${}^6\text{He}$  is  $r_{\text{mat}} = 2.43$  fm in our work (based on the 1.495 fm rms matter radius of  $\alpha$  cluster) and the corresponding  $r_{\text{mat}} = 2.46$  fm can be found in Ref. [6]. The difference here is not that large. Thus we have to presume very different geometry of  ${}^6\text{He}$  in the work [6]: the rms distance between two neutrons recalculated from  $r_\alpha$  and  $r_{\text{mat}}$  is  $r_{nn} = 3.11$  fm. This is drastically smaller than the value  $r_{nn} = 4.49$  fm used in present work. In general, the values  $r_{nn} > 4.3$  fm are typically found in all other model calculations of  ${}^6\text{He}$ .

The  ${}^6\text{He}$   $E1$  SF of Refs. [7,8] noticeably differs from our SF and from SF in Refs. [4,9]. Namely, the low-energy behavior of the SF in Refs. [7,8] is strongly enhanced compared to the HH-based works. Such a behavior is very difficult to reproduce in realistic calculations. This is an important issue since astrophysical capture rates are very sensitive to the low-energy behavior of the SF in a broad range of temperatures of interest. Therefore, we will return to this problem in a forthcoming paper [20]. It seems that all the methods collected in Fig. 14(b) have problems with correct treatment of the low-energy part of the  $E1$  SF in  ${}^6\text{He}$ . All these SFs tend at  $E_T \rightarrow 0$  either to constant, or to something visually different from the expected behavior of Eq. (27), see Fig. 14(a).

The correlation aspect of the SDM in  ${}^6\text{He}$  has been fragmentarily discussed in Refs. [5,10]. The results of Ref. [5] we discuss below when comparing with experimental data. In Ref. [10] the inclusive  $E_{n-n}$  and  $E_{\text{core-n}}$  distributions were constructed for the Coulomb breakup reaction. No comparison of this information with our results is possible.

## VII. COMPARISON WITH EXPERIMENTAL DATA

The results of the  ${}^6\text{He}$   $E1$  dissociation calculations are compared with available experimental data in Fig. 15 for SF and in Figs. 16, 17 for fragment correlations. Our SF, as well as other predictions [4–7], are consistent with each other and with experimental data [12] for  $E_T > 2$  MeV. However, for lower energies there is strong disagreement between experiment and all the calculations. There are certain differences in details, which we discussed above, but all the theoretical calculations in Fig. 15 predict a pronounced peak of  $E1$  SF in  ${}^6\text{He}$  at  $E_T \approx 0.9$ – $1.25$  MeV with peak values in the range  $\approx 0.27$ – $0.33$   $e^2\text{fm}^2/\text{MeV}$ . This feature of all the existing calculations disagrees with data far beyond the experimental uncertainty declared in Ref. [12].

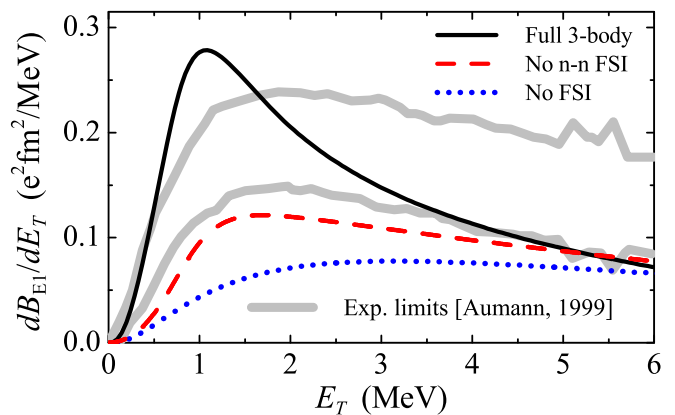


FIG. 15. Comparison of the results for the  ${}^6\text{He}$   $E1$  SF obtained in present work with experimental data [12].

Let us take a look at the correlation patterns observed for the  $E1$  dissociation of  ${}^6\text{He}$  in the experiment Ref. [12] and later published in Ref. [14]. It should be understood that the theoretical distributions are shown together with experimental data as is, without any accounting for the experimental bias, so this comparison can not be truly quantitative. Nevertheless, in Figs. 16 and 17 we may see that the agreement of the theoretical correlations with experimental data significantly improves, compared to the predictions of Ref. [5]. For example, there was a strong qualitative disagreement between theory of Ref. [5] and experiment in Figs. 16(b), 16(c) which is cured in our modern calculations.

There is, however, a considerable disagreement with the experimental data in correlations, which we should emphasize. The data is much smaller than theory in the energy

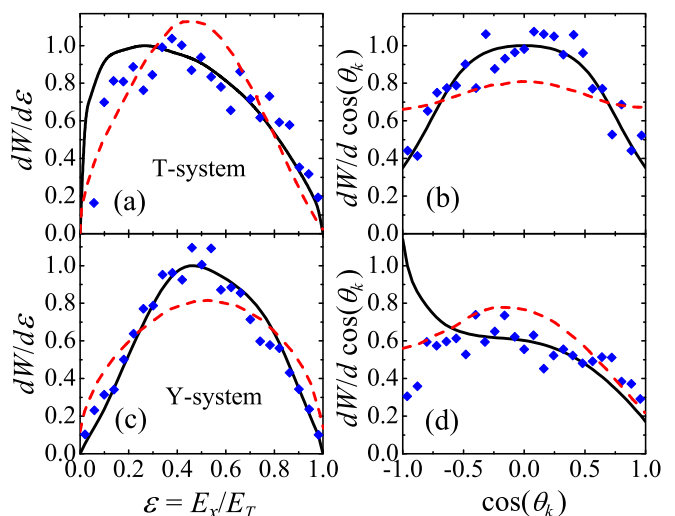


FIG. 16. The energy (a), (c) and angular (b), (d) distributions for products of the  $E1$  dissociation of  ${}^6\text{He}$  in T (a), (b) and Y (c), (d) Jacobi coordinate systems obtained in the continuum energy region  $E_T = 1$ – $3$  MeV. The experimental data from Ref. [14] are shown by diamonds. The solid black curves correspond to the calculation results of present work. The red dashed curves show the results of model Ref. [5] as given in Ref. [14].

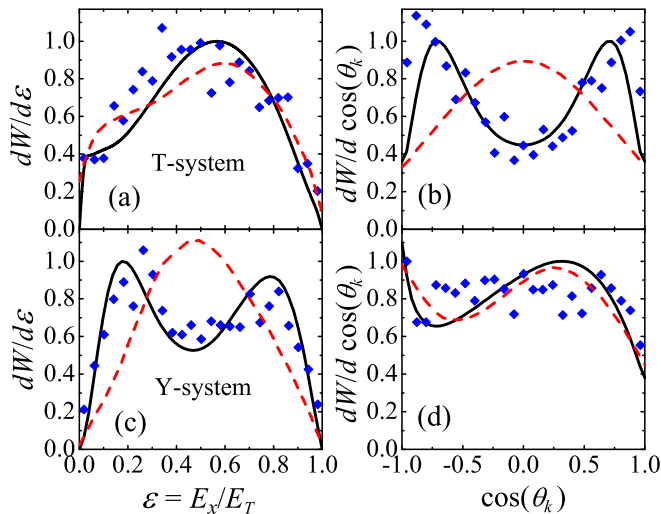


FIG. 17. The same as in Fig. 16, but for the continuum energy region  $E_T = 3\text{--}6$  MeV.

distribution Fig. 16(a) for  $\varepsilon < 0.3$  and in the angular distribution Fig. 16(d) for  $\cos(\theta_k) < -0.6$ . Both these ranges correspond to the same physical situation of low momentum between two neutrons. One may see in Fig. 7(a) that the energy distribution around  $E_T \approx 1$  MeV has a pronounced low-energy  $n\text{-}n$  peak (at higher  $E_T$  energies the low-energy  $n\text{-}n$  correlation is suppressed, see also Fig. 12). If we assume that the efficiency of the registration of the low-energy two-neutron events was underestimated in the data treatment of Ref. [12], then both of these disagreements in correlations and the absence of the  $E_T \approx 1$  MeV peak in experimental reconstructed strength function in Fig. 15 get explanation. To clarify this issue new high-precision experiments dedicated to SDM in  ${}^6\text{He}$  are necessary.

### VIII. CONCLUSIONS

Accurate calculations of the  $E1$  strength function (or soft dipole mode) for  ${}^6\text{He}$  are presented in this work. The results of these calculations significantly improved the older results of

the same collaboration Ref. [5]. Both the  $E1$  strength function and three-body decay correlation pattern are found to be fully converged for  $E_T > 0.1$  MeV. Fully converged results of this work allow us to understand strange wavy behavior of the  $E1$  SF predicted in theoretical papers [3,4,9] and corresponding strong disagreement among them. For the first time we are able to get insight for the decay dynamics for the soft dipole excitations. The transition from true three-body decay dynamics to sequential decay mechanism is taking place in the energy range  $E_T = 1.0\text{--}2.5$  MeV, which is reflected in the evolution of the correlation patterns.

It was demonstrated that the SDM results, obtained in this work, have important advantages compared to the other available theoretical calculations. However, the interpretation of the soft dipole excitation is a fragile issue, very sensitive to details of the models. Therefore the theoretical results have to be confirmed by the experimental data. Unfortunately, there is no agreement between  $E1$  SF for  ${}^6\text{He}$  obtained in the calculations and the  $E1$  strength function extracted from the  ${}^6\text{He}$  Coulomb dissociation cross section on the heavy target for the low-energy range  $E_T < 2$  MeV. This is true not only for our calculations, but for all the theoretical results available so far. Such a situation is unsatisfactory, since the radiative capture rates in nuclear astrophysics can be obtained only by the extrapolation based on the Coulomb dissociation cross section data. This is exactly the low-energy range, where the quality of the data are crucial for extrapolation to energies of astrophysical interest.

Intensive  ${}^6\text{He}$  beams are easily accessible at the modern RIB facilities, so it would be expected that the measurements with  ${}^6\text{He}$  should become a benchmark case for all the studies of this kind. So, highly precise measurements of the  $E1$  SF in  ${}^6\text{He}$  with modern techniques, as well as scrupulous comparison with theoretical calculations, taking the experimental bias into account, are very desirable.

### ACKNOWLEDGMENTS

L.V.G. and N.B.S. were supported in part by the Russian Science Foundation Grant No. 17-12-01367.

- 
- [1] N. Paar, D. Vretenar, E. Khan, and G. Colò, *Rep. Prog. Phys.* **70**, 691 (2007).
  - [2] D. Savran, T. Aumann, and A. Zilges, *Prog. Part. Nucl. Phys.* **70**, 210 (2013).
  - [3] B. V. Danilin and M. V. Zhukov, *Yad. Fiz.* **56**, 67 (1993) [*Phys. Atom. Nucl.* **56**, 460 (1993)].
  - [4] A. Cobis, D. V. Fedorov, and A. S. Jensen, *Phys. Rev. Lett.* **79**, 2411 (1997).
  - [5] B. Danilin, I. Thompson, J. Vaagen, and M. Zhukov, *Nucl. Phys. A* **632**, 383 (1998).
  - [6] T. Myo, K. Kato, S. Aoyama, and K. Ikeda, *Phys. Rev. C* **63**, 054313 (2001).
  - [7] R. de Diego, E. Garrido, D. Fedorov, and A. Jensen, *Europhys. Lett.* **90**, 52001 (2010).
  - [8] J. A. Lay, A. M. Moro, J. M. Arias, and J. Gómez-Camacho, *Phys. Rev. C* **82**, 024605 (2010).
  - [9] P. Descouvemont, E. Pinilla, and D. Baye, *Prog. Theor. Phys. Suppl.* **196**, 1 (2012).
  - [10] T. Myo, Y. Kikuchi, H. Masui, and K. Kato, *Prog. Part. Nucl. Phys.* **79**, 1 (2014).
  - [11] J. Singh, L. Fortunato, A. Vitturi, and R. Chatterjee, *Eur. Phys. J. A* **52**, 209 (2016).
  - [12] T. Aumann, D. Aleksandrov, L. Axelsson, T. Baumann, M. J. G. Borge, L. V. Chulkov, J. Cub, W. Dostal, B. Eberlein, T. W. Elze, H. Emling, H. Geissel, V. Z. Goldberg, M. Golovkov, A. Grünschloß, M. Hellström, K. Hencken, J. Holeczek, R. Holzmann, B. Jonson, A. A. Korshenninikov, J. V. Kratz, G. Kraus, R. Kulesa, Y. Leifels, A. Leistenschneider, T. Leth, I. Mukha, G. Münzenberg, F. Nickel, T. Nilsson, G. Nyman, B. Petersen, M. Pfützner, A. Richter, K. Riisager, C. Scheidenberger, G. Schrieder, W. Schwab, H. Simon, M. H. Smedberg, M. Steiner, J. Stroth, A. Surowiec, T. Suzuki,

- O. Tengblad, and M. V. Zhukov, *Phys. Rev. C* **59**, 1252 (1999).
- [13] T. Aumann, *Eur. Phys. J. A* **26**, 441 (2005).
- [14] L. V. Chulkov, H. Simon, I. J. Thompson, T. Aumann, M. J. G. Borge, T. W. Elze, H. Emling, H. Geissel, L. V. Grigorenko, M. Hellstrom, B. Jonson, J. W. V. Kratz, R. Kulesa, K. Markenroth, G. M. M. Meister, F. Nickel, T. Nilsson, G. Nyman, V. Pribora, K. R. A. Richter, C. Scheidenberger, G. Schrieder, O. Tengblad, and M. V. Zhukov, *Nucl. Phys. A* **759**, 23 (2005).
- [15] T. Nakamura, A. M. Vinodkumar, T. Sugimoto, N. Aoi, H. Baba, D. Bazin, N. Fukuda, T. Gomi, H. Hasegawa, N. Imai, M. Ishihara, T. Kobayashi, Y. Kondo, T. Kubo, M. Miura, T. Motobayashi, H. Otsu, A. Saito, H. Sakurai, S. Shimoura, K. Watanabe, Y. X. Watanabe, T. Yakushiji, Y. Yanagisawa, and K. Yoneda, *Phys. Rev. Lett.* **96**, 252502 (2006).
- [16] R. Kanungo, A. Sanetullaev, J. Tanaka, S. Ishimoto, G. Hagen, T. Myo, T. Suzuki, C. Andreoiu, P. Bender, A. A. Chen, B. Davids, J. Fallis, J. P. Fortin, N. Galinski, A. T. Gallant, P. E. Garrett, G. Hackman, B. Hadinia, G. Jansen, M. Keefe, R. Krücken, J. Lighthall, E. McNeice, D. Miller, T. Otsuka, J. Purcell, J. S. Randhawa, T. Roger, A. Rojas, H. Savajols, A. Shotter, I. Tanihata, I. J. Thompson, C. Unsworth, P. Voss, and Z. Wang, *Phys. Rev. Lett.* **114**, 192502 (2015).
- [17] J. Tanaka, R. Kanungo, M. Alcorta, N. Aoi, H. Bidaman, C. Burbadge, G. Christian, S. Cruz, B. Davids, A. D. Varela, J. Even, G. Hackman, M. Harakeh, J. Henderson, S. Ishimoto, S. Kaur, M. Keefe, R. Krücken, K. Leach, J. Lighthall, E. P. Rodal, J. Randhawa, P. Ruotsalainen, A. Sanetullaev, J. Smith, O. Workman, and I. Tanihata, *Phys. Lett. B* **774**, 268 (2017).
- [18] L. Grigorenko, K. Langanke, N. Shul'gina, and M. Zhukov, *Phys. Lett. B* **641**, 254 (2006).
- [19] Y. L. Parfenova, L. V. Grigorenko, I. A. Egorova, N. B. Shulgina, J. S. Vaagen, and M. V. Zhukov, *Phys. Rev. C* **98**, 034608 (2018).
- [20] L. V. Grigorenko, N. B. Shulgina, and M. V. Zhukov, *Phys. Lett. B* **807**, 135557 (2020).
- [21] A. Fomichev, V. Chudoba, I. Egorova, S. Ershov, M. Golovkov, A. Gorshkov, V. Gorshkov, L. Grigorenko, G. Kaminski, S. Krupko, I. Mukha, Y. Parfenova, S. Sidorchuk, R. Slepnev, L. Standylo, S. Stepantsov, G. Ter-Akopian, R. Wolski, and M. Zhukov, *Phys. Lett. B* **708**, 6 (2012).
- [22] B. V. Danilin, M. V. Zhukov, S. N. Ershov, F. A. Gareev, R. S. Kurmanov, J. S. Vaagen, and J. M. Bang, *Phys. Rev. C* **43**, 2835 (1991).
- [23] L. V. Grigorenko, R. C. Johnson, I. G. Mukha, I. J. Thompson, and M. V. Zhukov, *Phys. Rev. C* **64**, 054002 (2001).
- [24] L. V. Grigorenko, T. D. Wiser, K. Mercurio, R. J. Charity, R. Shane, L. G. Sobotka, J. M. Elson, A. H. Wuosmaa, A. Banu, M. McCleskey, L. Trache, R. E. Tribble, and M. V. Zhukov, *Phys. Rev. C* **80**, 034602 (2009).
- [25] M. V. Zhukov, B. Danilin, D. Fedorov, J. Bang, I. Thompson, and J. S. Vaagen, *Phys. Rep.* **231**, 151 (1993).
- [26] M. V. Zhukov, B. V. Danilin, L. V. Grigorenko, and N. B. Shul'gina, *Phys. Rev. C* **47**, 2937 (1993).
- [27] M. S. Golovkov, L. V. Grigorenko, A. S. Fomichev, Y. T. Oganessian, Y. I. Orlov, A. M. Rodin, S. I. Sidorchuk, R. S. Slepnev, S. V. Stepantsov, G. M. Ter-Akopian, and R. Wolski, *Phys. Lett. B* **588**, 163 (2004).
- [28] M. S. Golovkov, L. V. Grigorenko, A. S. Fomichev, S. A. Krupko, Y. T. Oganessian, A. M. Rodin, S. I. Sidorchuk, R. S. Slepnev, S. V. Stepantsov, G. M. Ter-Akopian, R. Wolski, M. G. Itkis, A. S. Denikin, A. A. Bogatchev, N. A. Kondratiev, E. M. Kozulin, A. A. Korshennikov, E. Y. Nikolskii, P. Roussel-Chomaz, W. Mittig, R. Palit, V. Bouchat, V. Kinnard, T. Materna, F. Hanappe, O. Dorvaux, L. Stuttgé, A. A. Yuhimchuk, V. V. Perevozchikov, Y. I. Vinogradov, S. K. Grishechkin, S. V. Zlatoustovskiy, V. Lapoux, R. Raabe, and L. Nalpas, *Phys. Rev. C* **72**, 064612 (2005).
- [29] S. I. Sidorchuk, A. A. Bezbakh, V. Chudoba, I. A. Egorova, A. S. Fomichev, M. S. Golovkov, A. V. Gorshkov, V. A. Gorshkov, L. V. Grigorenko, P. Jalůvková, G. Kaminski, S. A. Krupko, E. A. Kuzmin, E. Y. Nikolskii, Y. T. Oganessian, Y. L. Parfenova, P. G. Sharov, R. S. Slepnev, S. V. Stepantsov, G. M. Ter-Akopian, R. Wolski, A. A. Yuhimchuk, S. V. Filchagin, A. A. Kiryashkin, I. P. Maksimkin, and O. P. Vikhlyantsev, *Phys. Rev. Lett.* **108**, 202502 (2012).
- [30] V. Chudoba, L. V. Grigorenko, A. S. Fomichev, A. A. Bezbakh, I. A. Egorova, S. N. Ershov, M. S. Golovkov, A. V. Gorshkov, V. A. Gorshkov, G. Kaminski, S. A. Krupko, I. Mukha, E. Y. Nikolskii, Y. L. Parfenova, S. I. Sidorchuk, P. G. Sharov, R. S. Slepnev, L. Standylo, S. V. Stepantsov, G. M. Ter-Akopian, R. Wolski, and M. V. Zhukov, *Phys. Rev. C* **98**, 054612 (2018).
- [31] L. V. Grigorenko, M. S. Golovkov, S. A. Krupko, S. I. Sidorchuk, G. M. Ter-Akopian, A. S. Fomichev, and V. Chudoba, *Phys. Usp.* **59**, 321 (2016).
- [32] S. N. Ershov, L. V. Grigorenko, J. S. Vaagen, and M. V. Zhukov, *J. Phys. G: Nucl. Part. Phys.* **37**, 064026 (2010).
- [33] G. E. Brown and A. D. Jackson, *The Nucleon–Nucleon Interaction* (North-Holland, Amsterdam, 1976).
- [34] D. Gogny, P. Pires, and R. D. Tournel, *Phys. Lett. B* **32**, 591 (1970).
- [35] S. Sack, *Phys. Rev.* **93**, 321 (1954).
- [36] L. V. Grigorenko and M. V. Zhukov, *Phys. Rev. C* **76**, 014008 (2007).
- [37] B. V. Danilin and N. B. Shulgina, *Izv. Acad. Nauk SSSR Ser. Fiz.* **5**, 908 (1991).
- [38] L. V. Grigorenko and N. B. Shulgina, *Yad. Fiz.* **61**, 1582 (1998) [*Phys. At. Nucl.* **61**, 1472 (1998)].
- [39] I. A. Egorova, R. J. Charity, L. V. Grigorenko, Z. Chajecski, D. Coupland, J. M. Elson, T. K. Ghosh, M. E. Howard, H. Iwasaki, M. Kilburn, J. Lee, W. G. Lynch, J. Manfredi, S. T. Marley, A. Sanetullaev, R. Shane, D. V. Shetty, L. G. Sobotka, M. B. Tsang, J. Winkelbauer, A. H. Wuosmaa, M. Youngs, and M. V. Zhukov, *Phys. Rev. Lett.* **109**, 202502 (2012).
- [40] T. Golubkova, X.-D. Xu, L. Grigorenko, I. Mukha, C. Scheidenberger, and M. Zhukov, *Phys. Lett. B* **762**, 263 (2016).
- [41] K. W. Brown, R. J. Charity, L. G. Sobotka, Z. Chajecski, L. V. Grigorenko, I. A. Egorova, Y. L. Parfenova, M. V. Zhukov, S. Bedoor, W. W. Buhro, J. M. Elson, W. G. Lynch, J. Manfredi, D. G. McNeel, W. Reviol, R. Shane, R. H. Showalter, M. B. Tsang, J. R. Winkelbauer, and A. H. Wuosmaa, *Phys. Rev. Lett.* **113**, 232501 (2014).
- [42] K. W. Brown, R. J. Charity, L. G. Sobotka, L. V. Grigorenko, T. A. Golubkova, S. Bedoor, W. W. Buhro, Z. Chajecski, J. M. Elson, W. G. Lynch, J. Manfredi, D. G. McNeel, W. Reviol, R. Shane, R. H. Showalter, M. B. Tsang, J. R. Winkelbauer, and A. H. Wuosmaa, *Phys. Rev. C* **92**, 034329 (2015).

- [43] P. Egelhof, *Prog. Part. Nucl. Phys.* **46**, 307 (2001).
- [44] P. Mueller, I. A. Sulai, A. C. C. Villari, J. A. Alcántara-Núñez, R. Alves-Condé, K. Bailey, G. W. F. Drake, M. Dubois, C. Eléon, G. Gaubert, R. J. Holt, R. V. F. Janssens, N. Lécésne, Z.-T. Lu, T. P. O'Connor, M.-G. Saint-Laurent, J.-C. Thomas, and L.-B. Wang, *Phys. Rev. Lett.* **99**, 252501 (2007).
- [45] A. Ozawa, T. Suzuki, and I. Tanihata, *Nucl. Phys. A* **693**, 32 (2001).
- [46] S. Bacca, M. A. Marchisio, N. Barnea, W. Leidemann, and G. Orlandini, *Phys. Rev. Lett.* **89**, 052502 (2002).
- [47] D. Mikami, W. Horiuchi, and Y. Suzuki, *Phys. Rev. C* **89**, 064303 (2014).